Quality Control of Microwave Equipment for Tissue Imaging

Daniel Tajik, *Student Member, IEEE*, Jessica Trac, and Natalia K. Nikolova, *Fellow, IEEE*

***Abstract*—While the development of microwave imaging technology for biomedical applications has been ongoing for many years, no clinical devices are currently in use. A major challenge is achieving data quality that would ensure adequate image resolution for the specific diagnostic application. Imaging systems are typically designed with a theoretical resolution limit in mind, which is rarely achieved in practice due to measurement uncertainties, background clutter, and system noise. Uncertainties and background clutter are particularly prominent in medical diagnostic imaging. This paper proposes a method for data quality assessment of an experimental imaging system that aims at a specific image resolution. It utilizes two measurements, one of a uniform background medium and one of the same medium with a small scattering probe embedded within it. The probe's size and permittivity reflect the desired application-specific resolution. The method extracts the system point-spread function (PSF) from the two measurements and computes the PSF contrast-to-noise ratio. A case study is presented, demonstrating the quality control protocol and its ability to identify datasets of inadequate quality and provide an evaluation metric. The protocol also highlights possible sources of error and enables data filtering that increases significantly the reconstructed image quality.**

***Index Terms*—Microwave imaging, image quality, image resolution, signal to noise ratio, biomedical imaging, biomedical signal processing, biomedical image processing, quality management, quality control, calibration, contrast to noise ratio.**

I. Introduction

BIOMEDICAL microwave imaging technology shows promise in a variety of applications such as breast cancer imaging, stroke detection, skin cancer diagnosis, bone and joint imaging, and many more [1]–[10]. Microwave imaging technology is nonionizing, compact, and low-cost, demonstrating clear advantages over current diagnostic technology. These advantages motivate interest in developing microwave imaging as an alternative or complimentary diagnostic modality.

To date, however, microwave imaging technology has not been deployed in clinical practice. This is primarily due to the highly nonlinear scattering phenomenon in tissue [11]. A large number of algorithms have been developed to address these complexities, including direct (linear) and iterative (nonlinear) approaches, all of which employ approximations of the scattering behaviour [12]–[16]. While many of these approaches have appeared successful in studies with simulated data, their translation to successful experimental studies is limited.

In our experience, the difficulties arising in translation to practice are not necessarily due to the image reconstruction approach. Rather, the experimental setup fails to reproduce the idealized simulated acquisition environment. Factors such as reflections from components in the measurement setup, positioning uncertainties, uncertainties in the performance of the antennas and the electronics, system noise and inadequate calibration all cause misleading results during image reconstruction. Evaluating the ability of the experimental setup to provide data of adequate quality is therefore an essential first step toward translating an imaging method to clinical practice.

The process of evaluating diagnostic equipment is commonplace in medical diagnostics. It is referred to as quality assurance or quality control (QC) [17]–[19]. One common QC evaluation protocol identifies the actual spatial resolution of the system by acquiring the system-specific point spread function (PSF) [17]. A PSF describes the impulse response of an imaging system. It can be acquired through the measurement of a small scattering object within a uniform background medium. Complex QC protocols based on multiple scattering probes generating unique PSFs have been created to account for the numerous system-specific influences on the actual image resolution [20], [21]. These protocols ensure that the estimated theoretical resolution is physically achieved.

Designing an experimental microwave imaging system to achieve a particular estimate of resolution starts with four fundamental factors: frequency bandwidth, antenna beamwidth, spatial sampling, and frequency (or temporal) sampling [11]. Such an estimate, however, depends on simplifying assumptions such as uniform and open background medium as well as far-zone modes of propagation. These assumptions do not hold in microwave tissue imaging, which is a typical near-field scenario. Such non-ideal background conditions along with the simplifying approximations in the forward model of scattering necessitate a QC protocol for evaluating the actual system-specific resolution of the imaging system.

Here, we propose a QC protocol for evaluating the ability of an experimental system to achieve the resolution necessary to identify critical tissue targets (e.g., cancer). The protocol uses an algorithm which computes the contrast-to-noise ratio (CNR) of a PSF at each measurement frequency. A case study is performed

Manuscript received March 18, 2019; revised May 28, 2019; accepted June 25, 2019. Date of publication June 27, 2019; date of current version February 20, 2020. This work was supported by the Natural Sciences and Engineering Research Council of Canada (NSERC). *(Corresponding author: Daniel Tajik.)*

The authors are with the Electrical and Computer Engineering, McMaster University, Hamilton, ON L8S 4L8, Canada (e-mail: tajikd@mcmaster.ca; tracj2@mcmaster.ca; nikolova@ieee.org).

Digital Object Identifier 10.1109/JERM.2019.2925599

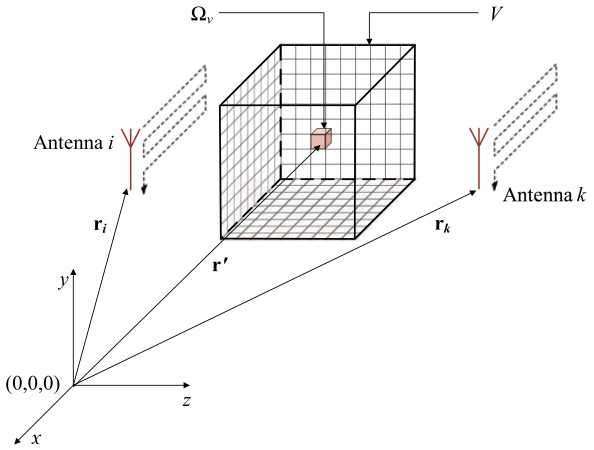

Fig. 1. Illustration of a planar acquisition setup. The antennas are scanned mechanically along the two parallel acquisition planes on both sides of the imaged volume V. If antennas i and k are both used as transmitting (Tx) and receiving (Rx) antennas, then the scattering parameters S_{ii}, S_{ik}, S_{ki}, S_{kk} are acquired as 2D complex-valued data sets at each frequency. Figure adapted from [37].

on the acquisition setup used for tissue-imaging experiments in [22]. The protocol also provides visual information to help determine the cause of poor CNR. The CNR QC protocol generates a metric which can be used to compare the current setup with similar acquisition systems.

II. Quality Control Protocol for Specified Resolution

The evaluated microwave imaging setup is a planar scanning system illustrated in Fig. 1. However, the QC protocol described next can be extended to systems employing cylindrical or hemispherical scanning surfaces and even surfaces of non-canonical shapes with nonuniform spatial sampling.

A. Point Spread Function Measurements

A point spread function (PSF) describes the impulse response of an imaging system. The PSF data consists of complex-valued scattering parameters from the measurement of a small scattering probe in a background medium, the volume of which includes the volume of a typical object-under-test (OUT). The protocol requires the measurement of two specifically constructed objects (phantoms) to derive the PSF: the reference object (RO) and the calibration object (CO).

The RO is a uniform phantom which fills the maximum capacity of the imaged volume V. Its measurement captures the incident-field response of the acquisition system, which includes system-specific features such as background clutter generated at interfaces between the equipment and surrounding air. The RO permittivity is designed to represent averaged tissue permittivity, weighted according to the percentage volume of each major tissue constituent in the anatomical model of the targeted organ. Note that the RO does not approximate complex tissue structures in the organ. Its purpose is to provide a baseline measurement in the absence of an OUT, which captures the dominant features of the system itself.

The CO phantom is comprised of: a) the uniform medium used in the RO measurement, and b) a scattering probe inserted within the uniform medium. The permittivity of the probe is selected to mimic a tissue structure of interest, e.g., a tumor. Its size corresponds to the desired spatial resolution. As an example, breast-cancer screening aims to detect sub-centimeter tumors [12]. Therefore, the size of the probe should be less than or equal to a cubic centimeter whereas the permittivity should approximate that of cancerous tissue. It is common for the permittivity of any given tissue type to have significant variance at any given frequency; e.g., for breast tumors, the real part of the relative permittivity may vary from 50 to 70 in the low-GHz range [23], [24]. The scattering probe permittivity is selected within this range.

A variety of tissue mimicking mixtures exist for designing the RO and CO structures. Oil-based phantoms can be easily constructed and maintained [25]–[28]. Carbon rubber mixtures have also shown reasonable success at achieving the required permittivities while also having substantial lifespans [29]–[31]. It should also be noted that many commercially available products (both organic and non-organic) appear to be viable candidates as long as their complex permittivity matches adequately the expected averaged tissue permittivity. Materials such as lard, peanut butter, and jam have been used in microwave phantoms [32]–[34]. This is not a novel approach; MRI phantoms are regularly designed using household items, including jams, jellies, and egg whites [35], [36].

The scattering probe is usually placed at the center of the imaged domain V, which is also the center of the RO and CO phantoms. We note that it is beneficial to place the scattering probe at different locations within the uniform phantom since different positions may correspond to somewhat different spatial resolution estimates as dictated by the width of the PSF. However, this comes at the cost of increased measurement effort. For the purposes of this work, CO measurements with a single probe position are carried out since the planar-scanning setup, where the antennas are aligned along boresight, features a PSF that is rather insensitive to the location of the probe.

B. Formulating the Point Spread Function

When the CO data set is measured, the total measured response is due to: a) scattered waves due to the scattering probe, and b) incident waves, which are independent of the probe and which form the baseline measurement. Only the scattered portion of the signal carries information about the scatterer; thus, it needs to be extracted from the total-field response. In the case of the PSF measurement, its scattered-field portion, $S_{ik}^{\mathrm{sc,PSF}}(\mathbf{r};f)$, can be extracted assuming a simple superposition of the incident and scattered field components [11]:

$$S_{ik}^{\mathrm{sc,PSF}}(\mathbf{r};f) \approx S_{ik}^{\mathrm{tot,CO}}(\mathbf{r};f) - S_{ik}^{\mathrm{RO}}(\mathbf{r};f)\,. \tag{1}$$

Here, $S_{ik}^{\mathrm{tot,CO}}(\mathbf{r};f)$ is the total measured response of the CO, and $S_{ik}^{\mathrm{RO}}(\mathbf{r};f)$ is the measured response of the RO.

The subtraction of the RO data from the total data aims at de-embedding the undesirable impact of the background measurement, which, in practice, is neither uniform nor perfectly

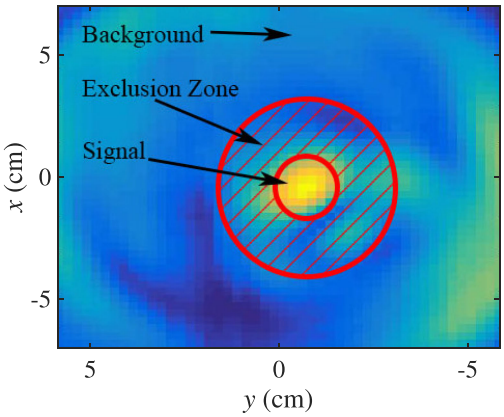

Fig. 2. Magnitude plot of acquired 2D PSF data at one frequency. Three regions are highlighted: (a) the signal region, (b) the background region, and (c) the exclusion region. Image adapted from [22].

repeatable. This issue is a major contributor to the measurement uncertainties of the particular system. The RO (or baseline) measurement is commonplace in microwave imaging and it is a mandatory step in the calibration of the system before proceeding with imaging an OUT [11].

Eq. (1) is a simple and widely used approach to the extraction of the scattered portion of a response. It is based on the first-order Born approximation [11]. However, using Rytov's approximation of scattering [11] is equally effective in the case of a PSF response. Details on the implementation of the Rytov data approximation are found in [32], [37], [38].

C. Contrast-to-Noise Ratio of the PSF

To evaluate the PSF measurement, each data set (for a given antenna pair and frequency) is divided into three regions of interest, as shown in Fig. 2: the signal region (A_s), the background region (A_b), and the exclusion region (A_e). The signal region A_s is the location where the majority of the scattered signal power is located. It is defined as all the voxels where the signal strength is within the 3 dB level relative to the maximum signal magnitude. The background region A_b is defined as the largest possible region containing no signal from the scattering probe. The exclusion region A_e is the region where the signal and noise components are difficult to separate. In A_e, ripple-like diffraction effects exists and they must be avoided in the CNR calculations described next.

In the context of this work, the signal-to-noise ratio (SNR) of a data set should be defined as

$$\mathrm{SNR}(f) = \frac{\mathrm{average}\left(S_{ik}^{\mathrm{tot,CO}}(A_\mathrm{s}, f)\right)}{\mathrm{std}(S_{ik}^{\mathrm{tot,CO}}(A_\mathrm{b}, f))}, A_\mathrm{s}, A_\mathrm{b} \in D \qquad (2)$$

where $S_{ik}^{\mathrm{tot,CO}}(A_\mathrm{s})$ is the total-field response in the signal region A_s contained within the scanned 2D domain D and $S_{ik}^{\mathrm{tot,CO}}(A_\mathrm{b})$ is the total-field response in the background region A_b. Here, std denotes the standard deviation function. As shown in [39], the average value and the standard deviation are calculated to produce real-positive values as:

$$\mathrm{average}(\boldsymbol{d}) = \left|\frac{1}{N}\sum_{i=1}^{N} d_i\right|, \qquad (3)$$

$$\mathrm{std}(\boldsymbol{d}) = \left(\frac{1}{N-1}\sum_{i=1}^{N}|d_i - \bar{d}|^2\right)^{\frac{1}{2}}, \bar{d} = \frac{1}{N}\sum_{i=1}^{N} d_i, \qquad (4)$$

where d_i is a single measurement at a particular location in the specified region (an element of the data vector $\boldsymbol{d}$), and N is the number of elements in $\boldsymbol{d}$.

In imaging, SNR can be a misleading metric, especially in cases where the incident-field component is stronger than the scattered-field component. This is because the reconstruction algorithm works with a signal which, ideally, contains only a scattered-field component. Therefore, using the scattered-field portion of the data sets is preferable.

Unfortunately, the incident-field response cannot be de-embedded from the PSF data completely, in part due to the near-field nature of the measurement, for which the superposition assumption in Eq. (1) does not hold strictly. The measurement uncertainties have a detrimental effect as well. Thus, instead of the SNR, a similar metric, referred to as the contrast-to-noise ratio (CNR), is preferable [22]:

$$\mathrm{CNR}(f) = \frac{\mathrm{average}(S_{ik}^{\mathrm{sc,PSF}}(A_\mathrm{s}, f)) - \mathrm{average}(S_{ik}^{\mathrm{sc,PSF}}(A_\mathrm{b}, f))}{\mathrm{std}(S_{ik}^{\mathrm{sc,PSF}}(A_\mathrm{b}, f))}, \qquad (5)$$

$$A_\mathrm{s} \in D, A_\mathrm{b} \in D.$$

Here, the average and the standard deviation are computed using Eqs. (3) and (4), respectively. The CNR measures the contrast between the scattered signal averaged over the signal region A_s and that averaged over the background region A_b, relative to the random contrasts (artifacts defining the data noise) that appear in the background region. Thus, CNR is insensitive to the incident-field responses which may not be removed completely during the de-embedding process.

After calculating the CNR for all data sets, a cut-off CNR is applied to determine whether a data set satisfies the QC requirements. Depending on the image-reconstruction algorithm, different CNR thresholds can be applied. In the case of quantitative microwave holography, a 3-dB threshold is suitable for determining whether the data quality is sufficient to accurately image scattering objects of the size and contrast similar to those of the scattering probe [22]. In a situation where 50% of the PSF data sets have a CNR below 3 dB, the system-specific resolution is deemed insufficient. In such cases, visual inspection of the two measured data sets (CO and RO) should be performed to identify system faults. As demonstrated in the case study described in Section III, such system faults can be usually remedied with simple modifications of the setup. A metric describing the overall system quality can be acquired from the mean CNR.

D. Quality Assurance Protocol

The CNR-based QC protocol can be summarized as follows:

1) Perform a measurement of the RO (uniform tissue mimicking phantom) to acquire $S_{ik}^{\mathrm{RO}}(\mathbf{r}, f)$.
2) Perform a measurement of the CO (uniform tissue mimicking phantom identical to the RO with a scattering probe embedded in the center) to acquire $S_{ik}^{\mathrm{tot,CO}}(\mathbf{r}, f)$.
3) Acquire the PSF $S_{ik}^{\mathrm{sc,PSF}}(\mathbf{r}, f)$ using Eq. (1).
4) At each frequency, identify the three regions of interest, referred to as the signal region A_{s}, the exclusion region A_{e}, and the background region A_{b}
5) Compute the CNR of each PSF data set using (5).
   a) If 50% of the PSF data sets have a CNR above the 3 dB threshold, the acquisition setup has sufficient quality at the particular system-specific resolution.
   b) If 50% of the PSF frequencies have a CNR below the 3 dB threshold, the acquisition setup has insufficient quality. Perform visual inspections of the CO and RO data. Return to step 1) after the experimental setup has been improved.

E. Algorithmic Implementation

An algorithmic approach is implemented in MATLAB [40] to automate the division of a PSF data set into *signal*, *background* and *exclusion* regions and to compute the CNR (available online [41]). Details of the implementation are provided in [42]. The algorithm operates on the PSF data obtained with Eq. (1).

To identify the signal region, the maximum signal strength is located, followed by the localization of all pixels of signal strength within -3 dB of the maximum. These pixels are organized into clusters. If multiple clusters are detected, the cluster closest to the center of the image is selected. The cluster selection uses a rectangular search region, which is centered within the acquisition area and has an initial size of 25% of the length and width of that area. If a cluster is not found in the initial search region, the algorithm increases the region in 5% increments until it reaches the size of the image. A warning is issued if the cluster is located outside of the initial search region since this implies that the scattering probe is not centered in the imaged volume or that significant measurement artifacts corrupt the PSF data. If the cluster approach fails to identify A_{s}, a backup approach defines the signal region as a circle with a user-defined radius, centered on the maximum-strength pixel.

Note that the cluster selection is prone to errors when a data set is corrupted by strong measurement artifacts. The baseline measurement of the uniform RO phantom may produce a nonuniform RO data set due to reflections from interfaces and interactions with the setup. These deviations from uniformity are referred to as measurement artifacts. When these artifacts are strong, they are not removed adequately via subtraction (see (1)), due to positioning errors, temperature changes, and other sources of uncertainty as discussed in Section III. As a result, multiple clusters of comparable strength may be present in the PSF, leading to uncertainty whether the algorithm has properly identified the signal region. In these scenarios, the CNR is always low (at or below 0 dB) due to the large variance in the background region. Thus, with poor quality data sets, the likelihood of the algorithm selecting the wrong "signal" cluster increases but this has little impact on the CNR which remains low regardless of the cluster selection.

Once the signal region A_{s} is identified, the exclusion region A_{e} is defined. This is accomplished by iteratively expanding a circular area which is centered on and is larger than A_{s}. The algorithm evaluates whether the variance of the signal (variance$(A) = \mathrm{std}(A)^2$) outside of A_{e}, i.e., within A_{b}, changes by more than a user-defined value. This user-defined value is based on the requirement that the percentage change in the signal variance within A_{b} must not exceed the percentage change in the size of A_{e}. For example, if the current iterate of A_{e} is expanded by 5% of the size of the acquisition area, and the variance in A_{b} changes by less than 4%, the search is considered to have converged and the previous iterate for the size of A_{e} is selected. The assumption is that the majority of the scattering signal due to the probe is contained within A_{s} and A_{e} whereas the background region A_{b} contains only noise, the variance of which does not depend on its size. The example percentage values above have been selected empirically for the planar scanning used in [22]. They can be redefined for a different setup as long as A_{b} contains minimum amount of diffraction effects. Once A_{s} and A_{b} are defined, (5) calculates the CNR for the data set.

III. Case Study

A planar raster scanning system, utilizing one transmitting TEM horn antenna [43] and 9-element receiving bowtie array [44], is evaluated for the purposes of breast-phantom imaging experiments performed in [22]. For simplicity, only the evaluation of the central antenna of the bowtie array is shown here since all antennas achieved similar CNR values. The frequency range is from 3 GHz to 8 GHz, in 100 MHz increments. The imaged volume is a 5 litre plexiglass ($\epsilon_r \approx 2 - \mathrm{i}0.1$) tray, the walls of which are 4 mm thick. It holds the embedding medium ($\epsilon_r \approx 10 - \mathrm{i}5$) and a compressed breast-tissue phantom. The antennas are connected to an R3970 Advantest 16 port RF switch and an Advantest 3770 Advantest vector network analyzer. An RF-Lambda 8-W power amplifier is connected to the transmitting antenna. The scanning system is placed within a custom microwave-absorber shielded chamber. The acquisition chamber can be seen in Fig. 3(a). The acquisition setup aims at detecting cancerous tissue approximately 1 cm^3 in size. In the case of planar scanning, the far-field resolution limits along *range* (z) and *cross-range* (x, y) are described by [11]:

$$\delta z \approx \frac{c_{\mathrm{b}}}{2 \cdot \mathrm{BW}}, \tag{6}$$

and

$$\Delta\zeta_{\max} \approx \frac{\lambda_{\min}}{4 \sin \alpha_{\max}}, \zeta \equiv x, y \tag{7}$$

where c_{b} is the speed of light in the background medium, BW is the frequency bandwidth, $\lambda_{\min}$ is the shortest wavelength of the radiation in the background medium, and $\alpha_{\max}$ is the largest angle of arrival (i.e., viewing angle) at which the scattered signal can be received. In practice, Eq. (7) is often approximated as

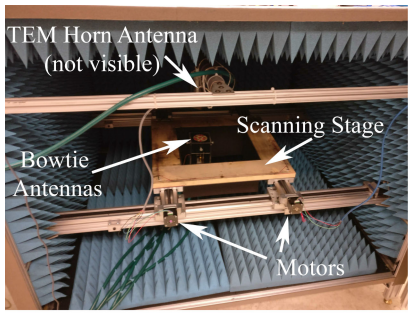

(a)

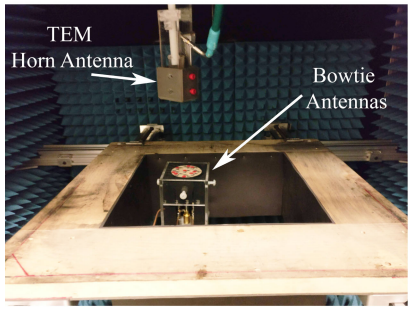

(b)

(c)

Fig. 3. Photos of the initial experimental setup: (a) the raster-scanning acquisition chamber in which the tray is placed, (b) inside the acquisition chamber, showing the TEM horn antenna and bowtie array aligned along boresight, and (c) a tray containing a uniform medium for the RO measurement.

$\Delta\zeta_{\max} = \frac{\lambda_{\min}}{2}$, which corresponds to an angle of arrival of 30° – a limit attributed to the antenna beamwidth or the aperture size, whichever results in a smaller $\alpha_{\max}$. In tissue, this assumption is reasonable regardless of the antenna beamwidths, bearing in mind that larger angles imply longer signal paths, leading to increasing signal attenuation. For this experiment, the range and cross-range theoretical resolution limits are estimated as $z \approx$ 9.5 mm and $\zeta \approx 6$ mm.

To verify the acquisition setup quality, the CNR QC protocol is performed. The permittivity of the uniform medium in the RO is based on a Type-2 breast, which is comprised of mostly fat with scattered fibroglandular tissue. The averaged permittivity of this tissue is expected to be $\epsilon_r \approx 10 - \mathrm{i}5$ at the central frequency of 5 GHz. The embedding medium, which is constructed from a mixture of peanut butter and jam (PBJ), is designed to achieved this permittivity [34]. The resultant mixture is measured with a Keysight (formerly Agilent) Technologies dielectric slim form

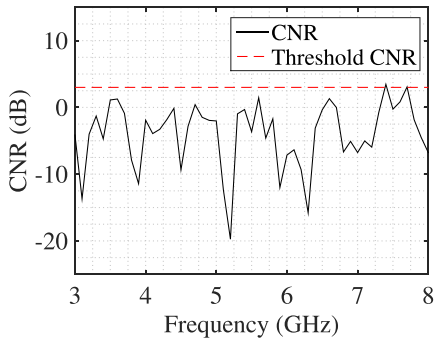

Fig. 4. Plot of the CNR values of the initial experimental setup. Most of the frequencies have CNR below the 3 dB threshold, indicating insufficient resolution for a 1-cm^3 scattering probe. The mean CNR is −2.13 dB.

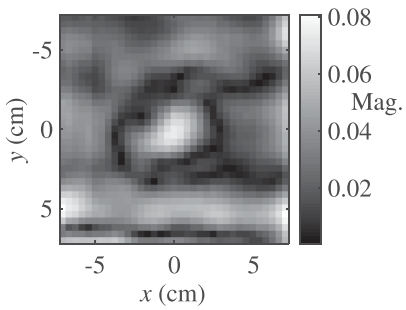

Fig. 5. Magnitude of the PSF data at 5.4 GHz. The data is obtained by subtracting the RO from from the CO data.

probe (85070E) to validate the mixture permittivity. The CO is constructed with the same uniform embedding medium, with the addition of a cylindrical dielectric scattering probe (diameter = 1 cm, height = 1 cm, $\epsilon_r \approx 50 - \mathrm{i}0.01$) placed in the center of the tray.

The CNR QC protocol described in Section II is applied and the initial CNR values of the central bowtie-array antenna are plotted *versus* frequency in Fig. 4. Most of the PSF data have CNR values below the 3 dB cutoff, indicating that the acquisition setup has insufficient resolution. The mean CNR of the data set is −2.13 dB. An example PSF (with the RO response de-embedded) at 5.4 GHz is shown in Fig. 5. Large interference patterns appear to track along the *x*-axis. The strength of one of these patterns is actually greater than that of the scattering probe (see the center of the domain). These interference patterns are also very apparent in the CO and RO data sets shown in Figs. 6 and 7, respectively.

The background de-embedding procedure through superposition (see Eq. (1)) fails to completely remove the interference patterns, possibly due to slight position misalignment of the tray in the CO and RO measurements. While positional error is important, such a significant interference pattern hints at a poor experimental design where improvement is necessary in terms of suppressing reflections in the background environment.

The cause of the interference is identified by the interference patterns aligned with the edges of the tray. Significant contrast exists between the embedding medium ($\epsilon_r \approx 10 - \mathrm{i}5$) and the

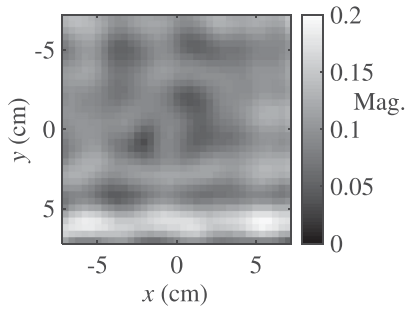

Fig. 6. Magnitude of the CO data set at 5.4 GHz.

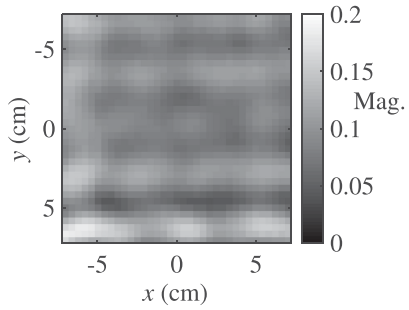

Fig. 7. Magnitude of the RO data set at 5.4 GHz.

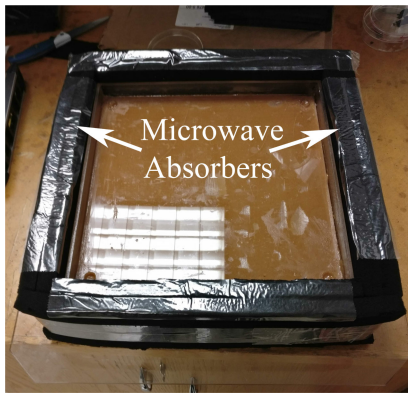

Fig. 8. Photo of the tray, showing the microwave absorbers that reduce reflections from the interface at the plexiglass walls.

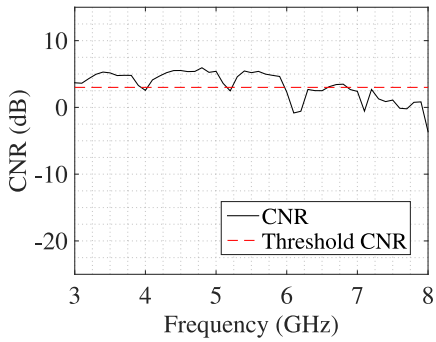

Fig. 9. Plot of the CNR values of the setup using microwave absorbers. Over 50% of the frequencies have CNR above 3 dB indicating that the system has sufficient resolution. As expected, the CNR at the higher frequencies is lower due to the increased signal attenuation – an effect not observed in Fig. 4 due to the overwhelming impact of background interference patterns. The mean CNR is 3.73 dB.

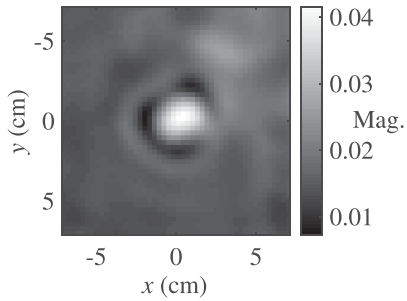

Fig. 10. Magnitude image of the PSF at 5.4 GHz after the addition of microwave absorbers to the tray in the experimental setup.

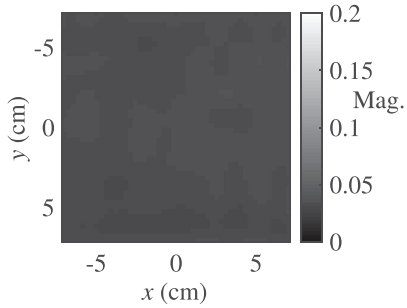

Fig. 11. Magnitude image of the RO after the addition of microwave absorbers to the tray in the experimental setup. It is scaled to match Fig. 7).

plexiglass walls ($\epsilon_r \approx 1$). This contrast induces significant reflections which produce the interference pattern visible in the CO and RO data sets.

To suppress reflections at the tray walls, microwave absorbing foam is placed around the tray. The foam is well matched to the low permittivity of the plexiglass and it leads to significant reduction of the background interference patterns. Fig. 8 depicts the tray containing uniform embedding medium with the microwave absorbing foam. The RO and CO measurements are performed again.

The CNR QC protocol is applied to the PSF data sets obtained from the new CO and RO data sets. The results are shown in Fig. 9. The CNR is now above the cutoff threshold of 3 dB for more than 50% of the frequencies. The mean CNR across all frequencies is 3.73 dB. At the same example frequency of 5.4 GHz, the PSF is far more clearly defined and no major interference pattern is visible (see Fig. 10). Indeed, the RO data at 5.4 GHz (see Fig. 11, scaled to match Fig. 7) no longer contains significant interference patterns. These results confirm that the modified acquisition setup has sufficient system-specific resolution.

Fig. 12 shows the magnitude of the PSF measured at 7.1 GHz, which has a CNR below the threshold. Note the presence of a measurement artifact in the top right of the image, which is stronger than that in Fig. 10. This leads to the reduced CNR. Fig. 12 also demonstrates the reduction of the overall signal strength as well as the size of the probe's scattering footprint at higher frequencies. It highlights a key trade-off in microwave

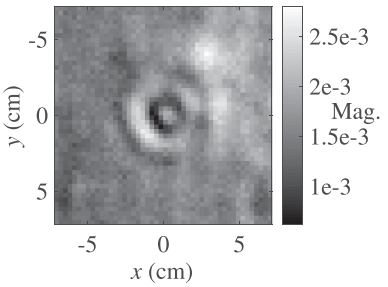

Fig. 12. Magnitude image of the PSF at 7.1 GHz after the addition of microwave absorbers to the tray in the experimental setup. Note that the CNR is lower due to significant contributions remaining in the background region of the PSF.

tissue imaging: higher frequencies facilitate higher resolution at the cost of lower signal strength.

Utilizing quantitative microwave holography [37], [45], a Fourier-based direct-inversion technique, image reconstruction of a breast tissue phantom has been performed with the modified acquisition setup [22]. The improved acquisition setup lead to successful imaging results discussed in detail in [22]. There, data filtering is applied to remove frequencies below the CNR threshold, leading to higher quality images.

IV. Discussion and Conclusions

A quality control (QC) approach for the evaluation of the system-specific resolution of an experimental setup for microwave tissue imaging is proposed. It utilizes the measurement of two separate structures (phantoms), and generates a system-specific point-spread function (PSF). The contrast-to-noise ratio (CNR) of the PSF is then calculated to determine if the signal quality is sufficient. If over 50% of the PSF data set have a CNR below 3 dB, the system has insufficient signal quality to resolve objects of size similar to that of the scattering probe. An algorithm evaluating the CNR is provided [41], [42], and a case study is performed with a planar microwave imaging acquisition used in [22]. The result demonstrates that the CNR QC protocol is able to identify insufficient resolution and to provide evidence pointing to the cause of poor signal quality. Addressing these causes leads to significant improvement of the system-specific resolution.

The CNR QC protocol generates a metric (mean CNR) which can be used to compare similar system implementations. This approach can be extended to multistatic setups in other antenna configurations including cylindrical and hemispherical arrangements. To implement the QC protocol, similar RO and CO structures need to be constructed and measured, where the permittivities and the probe's size would depend on the intended application. The scattering probe is usually placed in the center of the imaged volume. This placement does not provide an accurate resolution estimate for every position within the imaged domain, but represents a typical value which can be used to evaluate and compare imaging setups.

It is emphasized that the CNR metric must operate on the scattered portion of the CO response, which estimates the probe's impact on the measured responses and thus tests the sensitivity of the acquisition system to a very small source of scattering. There are reconstruction methods that operate on the scattered portion of the responses (e.g., microwave holography and synthetic focusing) and there are those that may operate on the total responses (e.g., microwave tomography). In both cases, however, the ability to measure reliably the difference between the background (the RO) response and that of the same background in the presence of a probe (the CO) is critical to the success of the reconstruction.

Finally, the protocol's definitions of *signal* and *background* regions in a PSF data set have been proposed and tested here for the case of planar acquisition surfaces. These definitions need to be modified for the cases of cylindrical and spherical acquisition surfaces. The modifications must preserve the physical meaning behind the concept so that *the signal region captures most of the scattering occurring at the probe* whereas *the background region captures most of the noise, clutter and uncertainty* occurring in the setup. For example, in the case of a spherical surface and with the probe being at the center of the imaged volume, the signal region would expand to include the PSF values at all sampling positions on this surface because they are equidistant from the probe. At the same time, the background region would also include all of these positions so that the PSF variance is extracted to give a measure of the deviation from the ideal uniform PSF distribution over the spherical surface. The cylindrical case would have both the signal and the background regions extending over all angular positions of the PSF whereas the vertical (axial) positions would require the separation of the two with a 1D variant of the method described in Section II-E.

A number of simple steps have been suggested to improve an experimental setup if the CNR QC protocol identifies an insufficient system-specific resolution. The addition of microwave absorbers around the antennas and other neighbouring structures reduces the impact of background clutter. Also, avoiding the use of system components such as plates and trays, which have high permittivity contrast with the objects being imaged, is beneficial. The use of an embedding medium for tissue measurements is very important since air-to-skin interfaces cause significant reflections and lower the signal penetration into the tissue.

Future work aims at two major objectives: a) methods for identifying the sources of error from measurement artifacts and b) developing and testing standard quality-control metrics for all microwave tissue imaging approaches, including those employing cylindrical and spherical acquisition surfaces. The first objective addresses a variety of errors including positional error, cabling/antenna uncertainties, calibration error, and system noise. The second objective requires extensive testing to ensure fair comparison among all acquisitions, and is entirely driven by the quality of the measured data, independent of the reconstruction method (i.e., how these data are processed).

In addition, designing calibration objects with several uncoupled scattering probes of varying sizes and contrasts can provide secondary metrics which more precisely characterize the system. A common QC metric in MRI evaluates the low-contrast detection capability using low-contrast probes [17]. Standardized QC structures have also been constructed for MRI, which utilize a number of different scattering probes of different shapes and

contrasts. The design of similar QC structures for microwave tissue-imaging systems would provide a standardized tool for the evaluation and comparison of emerging prototypes, thus pushing this technology towards successful implementation in clinical settings.

REFERENCES

[1] E. C. Fear, P. M. Meaney, and M. A. Stuchly, "Microwaves for breast cancer detection?" *IEEE Potentials*, vol. 22, no. 1, pp. 12–18, Feb. 2003.

[2] E. Porter, M. Coates, and M. Popović, "An early clinical study of time-domain microwave radar for breast health monitoring," *IEEE Trans. Biomed. Eng.*, vol. 63, no. 3, pp. 530–539, Mar. 2016.

[3] D. O'Loughlin, M. O'Halloran, B. M. Moloney, M. Glavin, E. Jones, and M. A. Elahi, "Microwave breast imaging: Clinical advances and remaining challenges," *IEEE Trans. Biomed. Eng.*, vol. 65, no. 11, pp. 2580–2590, Nov. 2018.

[4] D. Wörtge *et al.*, "Comparison of X-ray-mammography and planar UWB microwave imaging of the breast: First results from a patient study," *Diagnostics*, vol. 8, no. 3, Aug. 2018.

[5] D. Ireland, K. Bialkowski, and A. Abbosh, "Microwave imaging for brain stroke detection using born iterative method," *IET Microw. Antennas Propag.*, vol. 7, no. 11, pp. 909–915, Aug. 2013.

[6] R. Scapaticci, L. D. Donato, I. Catapano, and L. Crocco, "A feasibility study on microwave imaging for brain stroke detection," *Prog. Electromagn. Res. B*, vol. 40, pp. 305–324, Mar. 2012.

[7] I. Bisio *et al.*, "A numerical study concerning brain stroke detection by microwave imaging systems," *Multimedia Tools Appl.*, vol. 77, no. 8, pp. 9341–9363, Apr. 2018.

[8] P. Mehta, K. Chand, D. Narayanswamy, D. G. Beetner, R. Zoughi, and W. V. Stoecker, "Microwave reflectometry as a novel diagnostic tool for detection of skin cancers," *IEEE Trans. Instrum. Meas.*, vol. 55, no. 4, pp. 1309–1316, Aug. 2006.

[9] S. M. Salvador, E. C. Fear, M. Okoniewski, and J. R. Matyas, "Exploring joint tissues with microwave imaging," *IEEE Trans. Microw. Theory Techn.*, vol. 58, no. 8, pp. 2307–2313, Aug. 2010.

[10] P. M. Meaney *et al.*, "Clinical microwave tomographic imaging of the calcaneus: A first-in-human case study of two subjects," *IEEE Trans. Biomed. Eng.*, vol. 59, no. 12, pp. 3304–3313, Dec. 2012.

[11] N. K. Nikolova, *Introduction to Microwave Imaging*. Cambridge, U.K.: Cambridge Univ. Press, 2017.

[12] N. K. Nikolova, "Microwave imaging for breast cancer," *IEEE Microw. Mag.*, vol. 12, no. 7, pp. 78–94, Dec. 2011.

[13] R. Conceiçao, M. O'Halloran, and J. Mohr, *An Introduction to Microwave Imaging for Breast Cancer Detection*. New York, NY, USA: Springer, Jul. 2016.

[14] A. C. Kak and M. Slaney, *Principles of Computerized Tomographic Imaging*. Philadelphia, PA, USA: Soc. Ind. Appl. Math., 1988.

[15] S. Kwon and S. Lee, "Recent advances in microwave imaging for breast cancer detection," *Int. J. Biomed. Imag.*, vol. 2016, p. 26, Oct. 2016.

[16] K. D. Paulsen, P. M. Meaney, and L. C. Gilman, *Alternative Breast Imaging: Four Model-Based Approaches*. Springer US: New York, NY, USA, 2004.

[17] M. J. Firbank, R. M. Harrison, E. D. Williams, and A. Coulthard, "Quality assurance for MRI: practical experience," *Brit. J. Radiol.*, vol. 73, no. 868, pp. 376–383, 2000.

[18] R. R. Price *et al.*, "Quality assurance methods and phantoms for magnetic resonance imaging: Report of AAPM nuclear magnetic resonance Task Group No. 1," *Med. Phys.*, vol. 17, no. 2, pp. 287–295, 1990. [Online]. Available: https://aapm.onlinelibrary.wiley.com/doi/abs/10.1118/1.596566

[19] R. T. Droege, "A quality assurance protocol for CT scanners," *Radiology*, no. 146, pp. 244–246, Jan. 1983.

[20] T. M. Ihalainen *et al.*, "MRI quality assurance using the ACR phantom in a multi-unit imaging center," *Acta Oncologica*, vol. 50, no. 6, pp. 966–972, 2011.

[21] P. Judy, S. Balter, D. Bassano, E. McCullough, J. Payne, and L. Rothenberg, *Phantoms for Performance Evaluation and Quality Assurance of CT Scanners*, 1st ed. Alexandria, VA, USA: American Association of Physicists in Medicine (AAPM), 1977.

[22] D. Tajik, J. Trac, and N. K. Nikolova, "Spatial resolution evaluation of a microwave system for breast cancer screening," in *Proc. 13th Eur. Conf. Antennas Propag.*

[23] A. Martellosio *et al.*, "Dielectric properties characterization from 0.5 to 50 ghz of breast cancer tissues," *IEEE Trans. Microw. Theory Techn.*, vol. 65, no. 3, pp. 998–1011, Mar. 2017.

[24] M. Lazebnik *et al.*, "A large-scale study of the ultrawideband microwave dielectric properties of normal, benign and malignant breast tissues obtained from cancer surgeries," *Phys. Med. Biol.*, vol. 52, no. 20, pp. 6093–6115, 2007. [Online]. Available: http://stacks.iop.org/0031-9155/52/i=20/a=002

[25] M. O'Halloran *et al.*, "Development of anatomically and dielectrically accurate breast phantoms for microwave imaging applications," in *Proc. SPIE*, vol. 9077, 2014, Art. no. 90770Y.

[26] N. Joachimowicz, C. Conessa, T. Henriksson, and B. Duchâne, "Breast phantoms for microwave imaging," *IEEE Antennas Wireless Propag. Let.*, vol. 13, pp. 1333–1336, 2014.

[27] Y. Baskharoun, A. Trehan, N. K. Nikolova, and M. D. Noseworthy, "Physical phantoms for microwave imaging of the breast," in *Proc. IEEE Topical Conf. Biomed. Wireless Technol. Netw. Sens. Syst.*, Jan. 2012, pp. 73–76.

[28] A. Trehan, "Numerical and physical models for microwave breast imaging," Master of Appl. Sci. Thesis, Elect. Comput. Eng., McMaster Univ., Hamilton, ON, USA, 2009.

[29] J. Garrett and E. Fear, "Stable and flexible materials to mimic the dielectric properties of human soft tissues," *IEEE Antennas Wireless Propag. Lett.*, vol. 13, pp. 599–602, 2014.

[30] A. Santorelli, O. Laforest, E. Porter, and M. Popović, "Image classification for a time-domain microwave radar system: Experiments with stable modular breast phantoms," in *Proc. 9th Eur. Conf. Antennas Propag.*, Apr. 2015, pp. 1–5.

[31] J. Moll *et al.*, "Quality control of carbon-rubber tissue phantoms: Comparative MRI, CT, X-ray and UWB microwave measurements," in *Proc. 11th Eur. Conf. Antennas Propag.*, Mar. 2017, pp. 2723–2727.

[32] D. Tajik, D. S. Shumakov, and N. K. Nikolova, "An experimental comparison between the Born and Rytov approximations in microwave tissue imaging," in *Proc. IEEE Int. Microw. Symp.*, Jun. 2017, pp. 1391–1393.

[33] D. Tajik, D. S. Shumakov, A. S. Beaverstone, and N. K. Nikolova, "Quasi-real time reconstruction of the complex permittivity of tissue through microwave holography," in *Proc. 11th Eur. Conf. Antennas Propag.*, Mar. 2017, pp. 3485–3488.

[34] D. Tajik, F. Foroutan, D. S. Shumakov, A. D. Pitcher, and N. K. Nikolova, "Real-time microwave imaging of a compressed breast phantom with planar scanning," *IEEE J. Electromagn. RF Microw. Med. Biol.*, vol. 2, no. 3, pp. 154–162, Sep. 2018.

[35] G. P. Liney, D. J. Tozer, and L. W. Turnbull, "A simple and realistic tissue-equivalent breast phantom for MRI," *J. Magn. Reson. Imag.*, vol. 10, pp. 968–971, 1999.

[36] M. Freed *et al.*, "An anthropomorphic phantom for quantitative evaluation of breast MRI," *Med. Phys.*, vol. 38, no. 2, pp. 743–753, Feb. 2011. [Online]. Available: https://www.ncbi.nlm.nih.gov/pubmed/21452712

[37] D. Tajik, A. D. Pitcher, and N. K. Nikolova, "Comparative study of the Rytov and Born approximations in quantitative microwave holography," *Prog. Electromagn. Res. B*, vol. 79, pp. 1–19, Oct. 2017.

[38] D. S. Shumakov and N. K. Nikolova, "Fast quantitative microwave imaging with scattered-power maps," *IEEE Trans. Microw. Theory Techn.*, vol. 66, no. 1, pp. 439–449, Jan. 2018.

[39] J. J. McCombe and N. K. Nikolova, "SNR assessment of microwave imaging systems," in *Proc. IEEE Antennas Propag. Symp.*, Jul. 2014, pp. 149–150.

[40] "MATLAB Signal Processing Toolbox," The MathWorks, Natick, MA, USA, 2014.

[41] N. K. Nikolova, Matlab codes. Feb. 15, 2019. [Online]. Available: http://www.ece.mcmaster.ca/faculty/nikolova/IntroMicrowaveImaging/MatlabCodes

[42] J. Trac, "Classifying the quality of point spread functions with contrast-to-noise ratios," McMaster Univ., Hamilton, ON, Canada, Tech. Rep. EMVI-R-83, Aug. 2018. [Online]. Available: http://www.ece.mcmaster.ca/faculty/nikolova/IntroMicrowaveImaging/MatlabCodes/CNRevaluation/

[43] R. K. Amineh, A. Trehan, and N. K. Nikolova, "TEM horn antenna for ultra-wide band microwave breast imaging," *Prog. Electromagn. Res. B*, vol. 13, no. 13, pp. 59–74, Jan. 2009.

[44] R. K. Amineh, J. J. McCombe, A. Khalatpour, and N. K. Nikolova, "Microwave holography using point spread functions measured with calibration objects," *IEEE Trans. Instrum. Meas.*, vol. 64, no. 2, pp. 403–417, Feb. 2015.

[45] D. Tajik, J. R. Thompson, A. S. Beaverstone, and N. K. Nikolova, "Real-time quantitative reconstruction based on microwave holography," in *Proc. IEEE Int. Symp. Antennas Propag.*, Jun. 2016, pp. 851–852.

Daniel Tajik received the bachelor's degree in electrical and biomedical engineering and the master's degree in electrical and computer engineering from McMaster University, Hamilton, ON, Canada, in 2015 and 2017, respectively. His Ph.D. research is focused on developing microwave image processing algorithms for use in medical diagnostics. He is the Lead Ground Station Designer for McMaster NEUDOSE, a CubeSat project expected to launch in 2021. His interests include applications of microwave engineering in breast-cancer imaging, stroke detection, concealed weapon detection, and through-the-wall imaging. In 2017, he received both the First Place and Audience Choice Awards in the first ever 3MT competition at the IEEE International Microwave Symposium for his presentation "Microwave Holography: The Future of Medical Imaging." He is also the recipient of several major scholarhips, with the most recent being the three year Alexander Graham Bell Canada Graduate Scholarship-Doctoral, awarded in 2018.

Jessica Trac is currently an undergraduate student in electrical and biomedical engineering at McMaster University, Hamilton, ON, Canada, and will receive her Bachelor's degree in 2019. She is the recipient of three NSERC (Natural Sciences and Engineering Research Council of Canada) USRAs (Undergraduate Student Research Awards), which supported her research projects in medical imaging (breast-cancer microwave imaging, MRI permeability modelling) and neurorehabilitation (wearable technology) at McMaster University and the University of Toronto, Toronto, ON, Canada, respectively. Her interests include combining technology and engineering with medicine and clinical applications to improve diagnostics and patient care.

Natalia K. Nikolova (S'93'97–SM'05–F'11) received the Dipl. Eng. degree from the Technical University of Varna, Varna, Bulgaria, in 1989, and the Ph.D. degree from the University of Electro-Communications, Tokyo, Japan, in 1997. From 1998 to 1999, she held a Postdoctoral Fellowship of the Natural Sciences and Engineering Research Council of Canada (NSERC), during which time she was initially with the Microwave and Electromagnetics Laboratory, DalTech, Dalhousie University, Halifax, NS, Canada, and, later, for a year, with the Simulation Optimization Systems Research Laboratory, McMaster University, Hamilton, ON, Canada. In July 1999, she joined the Department of Electrical and Computer Engineering, McMaster University, where she is currently a Professor. She served as a Distinguished Microwave Lecturer from 2010 to 2013. Her research interests include inverse scattering and microwave imaging, theoretical and computational electromagnetism, as well as high-frequency computer-aided design. She currently serves on three IEEE Technical Coordinating Committees: MTT-1 (Computer-aided Design), MTT-10 (Biological Effects and Medical Applications), and MTT-15 (Microwave Field Theory). She was the recipient of a University Faculty Award of NSERC from 2000 to 2005. Since 2008, she is a Canada Research Chair in High-frequency Electromagnetics. She is a Fellow of the Canadian Academy of Engineering (CAE).